

# Cryogenic X-ray photoelectron spectroscopy for battery interfaces

Sanzeeda Baig Shuchi<sup>1</sup>, Giulio D'Acunto<sup>1</sup>, Philaphon Sayavong<sup>2</sup>, Solomon T. Oyakhire<sup>1†</sup>, Kenzie M. Sanroman Gutierrez<sup>1</sup>, Juliet Risner-Jamtgaard<sup>3</sup>, Yi Cui<sup>4,5,6\*</sup>, Stacey F. Bent<sup>1,6\*</sup>

<sup>1</sup>Department of Chemical Engineering, Stanford University; Stanford, CA, USA.

<sup>2</sup>Department of Chemistry, Stanford University; Stanford, CA, USA.

<sup>3</sup>Stanford Nano Shared Facilities, Stanford University; Stanford, CA, USA.

<sup>4</sup>Stanford Institute for Materials Energy and Energy Sciences, SLAC National Laboratory; Menlo Park, CA, USA.

<sup>5</sup>Department of Materials Science and Engineering, Stanford University; Stanford, CA, USA.

<sup>6</sup>Department of Energy Science and Engineering, Stanford University; Stanford, CA, USA.

†Present address: Department of Materials Science and Engineering, University of California Berkeley; Berkeley, CA, USA.

\*Corresponding Authors: S.F.B. [sbent@stanford.edu](mailto:sbent@stanford.edu), Y.C. [yicui@stanford.edu](mailto:yicui@stanford.edu)

## Abstract

Understanding the chemical environment of pristine interfaces is a long-sought goal in electrochemistry, materials science, and surface science. A substantial understanding of one such interface, the solid electrolyte interphase (SEI) in lithium anodes, originates from X-ray photoelectron spectroscopy (XPS). However, room temperature (RT) combined with ultra-high vacuum (UHV) can induce major SEI evolution from reactions and volatilization during XPS. Subsequently, a technique is necessary for SEI stabilization. Here, we develop cryogenic (cryo)-XPS with immediate plunge freezing and demonstrate SEI preservation. We discover completely different SEI speciation and a thicker pristine SEI with cryo-XPS, free from RT-associated thickness reduction and alterations to major species including LiF and Li<sub>2</sub>O in UHV. This new access to pristine SEI composition enables performance correlations across diverse electrolyte chemistries. Primarily, we highlight the necessity of studying sensitive interfaces under cryo conditions.

## Main

Electrode-electrolyte interfaces are pivotal for constructing high-performing electrochemical devices<sup>1-3</sup>. One significant example, the solid electrolyte interphase (SEI) in lithium (Li) batteries, is defined as the nanometer-thick passivation layer formed at the anode-electrolyte interface from electrolyte decomposition<sup>4,5</sup>. SEI is considered the most critical solid interphase in Li-ion and Li metal batteries<sup>4,6</sup>.

X-ray photoelectron spectroscopy (XPS) is the major technique for SEI chemical characterization due to its specific molecular species identification capability and nanoscale depth sensitivity,

contributing to most of our understanding of the SEI chemical environment<sup>7,8</sup>. However, SEI characterization with XPS is predominantly performed at room temperature (RT). At RT, spontaneous decomposition and growth reactions can alter SEI composition<sup>7,9–13</sup>. Moreover, the ultra-high vacuum (UHV) conditions of the XPS chamber ( $\lesssim 10^{-6}$  Pa) can reduce SEI thickness at RT through volatilization of SEI species and decomposition products<sup>7</sup>. Besides, beam damage of the SEI often occurs during X-ray and transmission electron microscopy (TEM) analyses<sup>12,14</sup>. Consequently, RT-XPS may not reflect what is truly at the interphase but rather depict an evolved interphase.

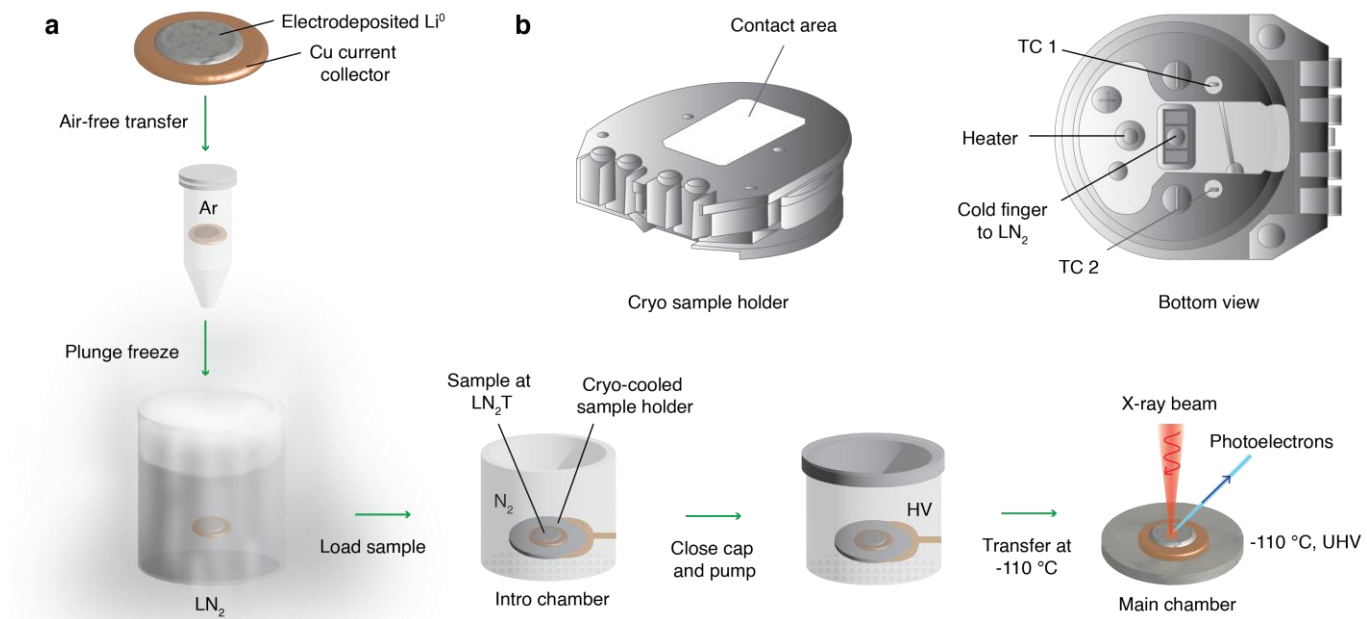


**Fig. 1. Cryo-XPS transfer process for SEI preservation.** **a**, Li metal is electrodeposited on a copper (Cu) current collector and then plunged into LN<sub>2</sub> instantly after sample preparation. The sample at LN<sub>2</sub>T is then placed onto the contact area of a cryo-cooled sample holder. The N<sub>2</sub> pressure, higher than ambient pressure, inside the intro chamber ensures an inert environment around the sample right before pumping. Transfer to the main chamber and spectra collection are performed at  $\sim 110$  °C. **b**, The cryo sample holder is cooled using the cold finger crimped to a Cu wire blade that leads to an LN<sub>2</sub> dewar. LN<sub>2</sub> denotes liquid nitrogen, HV denotes high vacuum, UHV denotes ultra-high vacuum, and TC denotes thermocouple.

Here, we develop cryogenic (cryo)-XPS transfer (Fig. 1, Methods) by plunge freezing the SEI sample instantly in liquid N<sub>2</sub> (LN<sub>2</sub>,  $\sim -196$  °C) to preserve the SEI in its pristine chemical state. We hypothesize that cryo-XPS can create valuable impacts to understand the detailed chemical environment of pristine SEI because cryogenic conditions can halt chemical reactions and freeze UHV-volatile species. Most chemical reactions are halted due to slow reaction kinetics at cryoT<sup>12,15</sup>. We hypothesize that the true SEI thickness can also be retained, benefiting from the lower vapor pressure of different frozen SEI species at cryoT. This is reasonable as we draw inspiration from cryo-EM, where cryo conditions have led to very fruitful discoveries on preserved

interfaces in batteries<sup>12,15–18</sup> and in biology<sup>19–25</sup>. Particularly, cryo-XPS can be highly impactful and complementary to cryo-EM for SEI characterization as it can offer information on detailed chemical speciation including different oxidation states. We perform spectra collection at  $\sim$ 110 °C (the minimum allowed temperature for our cryo holder), so the sample eventually warms up to  $\sim$ 110 °C, which we find to be sufficient to preserve the sample during analysis. We confirm the SEI thickness preservation from Li 1s high-resolution spectra.

### Time-dependent SEI preservation and evolution

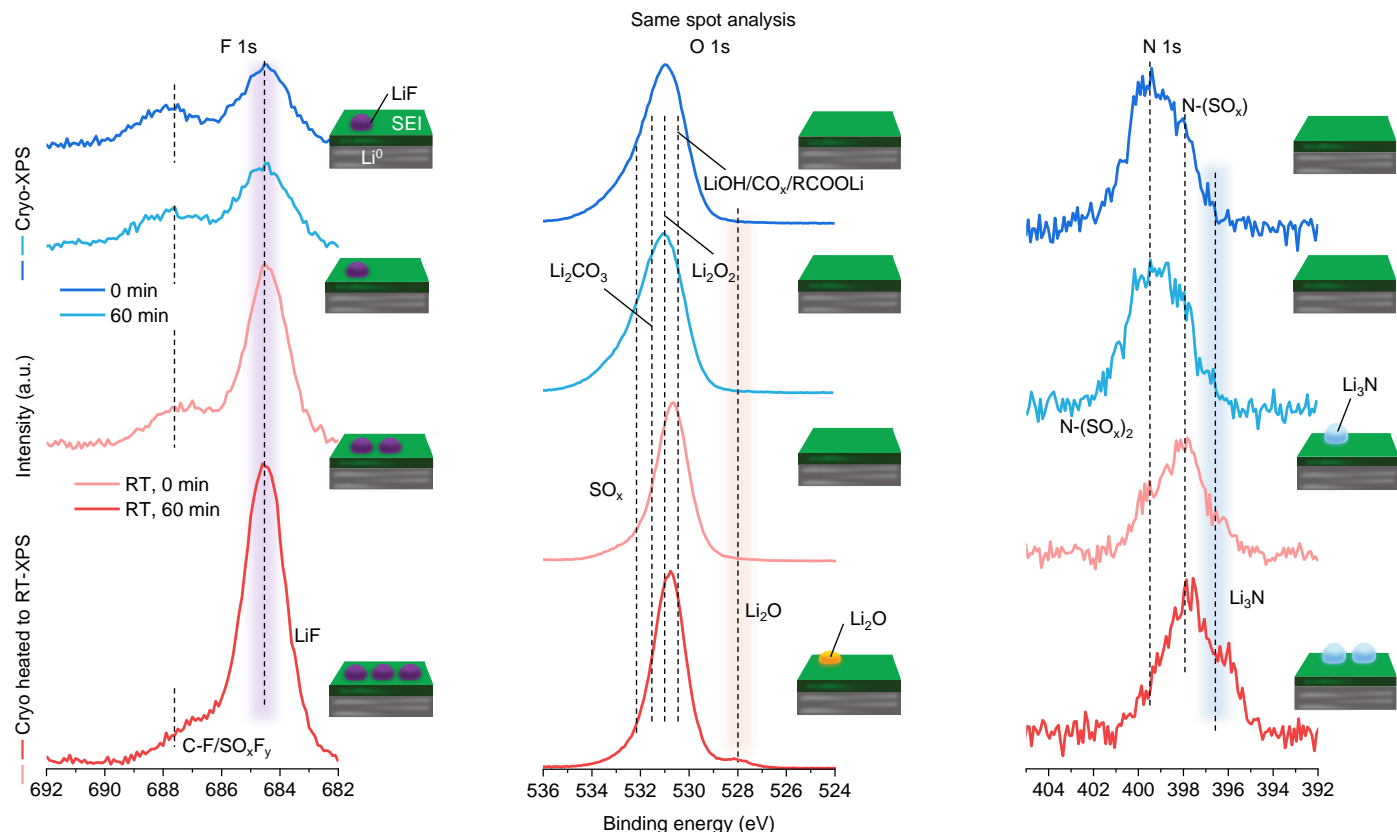


**Fig. 2. Time-dependent SEI preservation and evolution.** Time-resolved high-resolution spectra for F 1s, O 1s, and N 1s peaks with cryo-XPS and cryo heated to RT-XPS with schematics showing the evolution of LiF, Li<sub>2</sub>O, and Li<sub>3</sub>N species at 0 min and at 60 min. The measurements are carried out on one sample at the same spot to capture the SEI evolution decoupled from SEI spatial heterogeneities. The electrolyte used is 1 M LiFSI/DME. Spectra are normalized with respect to the SO<sub>x</sub>F<sub>y</sub>/C-F peak.

To understand the time-dependent SEI compositional changes during cryo-XPS and RT-XPS, we compare the time-resolved XPS data collected from the same analysis spot using a plunge frozen SEI sample with cryo-XPS and again after heating it to RT (Fig. 2). First, we notice that the high-resolution XPS spectra for the F 1s, O 1s, and N 1s peaks collected under cryo-XPS and UHV conditions remain similar as time passes (0 min and after 60 min). By contrast, after heating the sample to RT, major changes are observed when analyzing the same spot. After 60 min at RT, the composition of the same spot changes even further. This result is crucial and establishes the

preservation effect of cryo-XPS and the sample evolution effect of RT-XPS. Discussing the specific example for F 1s, increases in the intensity of the peak associated with LiF (~684.5 eV) are observed both upon reaching RT and after 60 min at RT. As species amount scales with peak intensity, the results suggest that cryo-XPS shows a relatively lower LiF amount and a time-invariant SEI composition. The relative LiF content increases once the SEI reaches RT. After an elongated stay at RT, the relative LiF content rises even further. Analogous preservation and evolution effects are observed for all the other SEI constituents, including inorganic species like Li<sub>2</sub>O and Li<sub>3</sub>N in O 1s and N 1s regions respectively (Fig. 2, Extended Data Fig. 1-2). A more pronounced effect is observed during RT-XPS of an unwashed SEI sample as it retains a larger quantity of reactive and volatile species from the electrolyte (Extended Data Fig. 3).

We further investigate the necessity of immediate plunge freezing and the reversibility of SEI evolution at RT by re-cooling the SEI to cryoT (Extended Data Fig. 4). The relative LiF content in the F 1s peak increases from cryo-XPS both after heating to RT and again after re-cooling sequentially. This result indicates that composition evolution at RT is irreversible and gradual cooling under vacuum does not preserve the SEI composition. Thus, plunge freezing the sample in liquid N<sub>2</sub> immediately after sample preparation is recommended.

#### *Reaction effect*

We study the reaction effect by comparing the SEI chemical composition under three experimental conditions, namely: cryo-XPS, *in situ* heating of the same sample to RT, and regular RT-XPS (Fig. 3a), each in high-performing localized high concentration electrolyte (LHCE) electrolyte. We consider F 1s and O 1s spectral regions due to LiF<sup>26–28</sup> and Li<sub>2</sub>O<sup>29,30</sup> being often discussed beneficial SEI species for improved cycling. Analogous to our previous observations from the F 1s peaks (Fig. 2, Extended Data Fig. 2-4), we find that both cryo heated to RT-XPS and regular RT-XPS yield a higher LiF peak intensity than cryo-XPS (F 1s region, Fig. 3a). So, it is generally concluded that performing RT-XPS analysis on the SEI leads to an overestimation of the amount of LiF in the SEI. This overestimation is misleading because higher LiF content is often associated with improved cycling performance<sup>26–28</sup>. The higher LiF peak intensity in the SEI at RT can be explained by several reactions and volatilization resulting in stable LiF as the remaining product (Supplementary Note 1). One possible reaction for this model SEI from LHCE leading to a stable LiF end product can progress via S-F bond cleavage of SO<sub>x</sub>F<sub>y</sub> species<sup>8</sup> written as,



The reaction effect for the SEI on Li can be explained by simultaneous SEI decomposition forming more stable products and SEI growth reactions from chemical corrosion of Li<sup>7,9–13</sup>. SEI decomposition reactions are more favorable than SEI growth atop a more noble Cu substrate in the absence of electrodeposited Li<sup>31</sup>. Even on Cu, we observe a drastic change in SEI composition between cryo and RT conditions toward higher LiF at RT (Extended Data Fig. 5), suggesting that SEI decomposition reactions may be the primary cause of composition evolution.

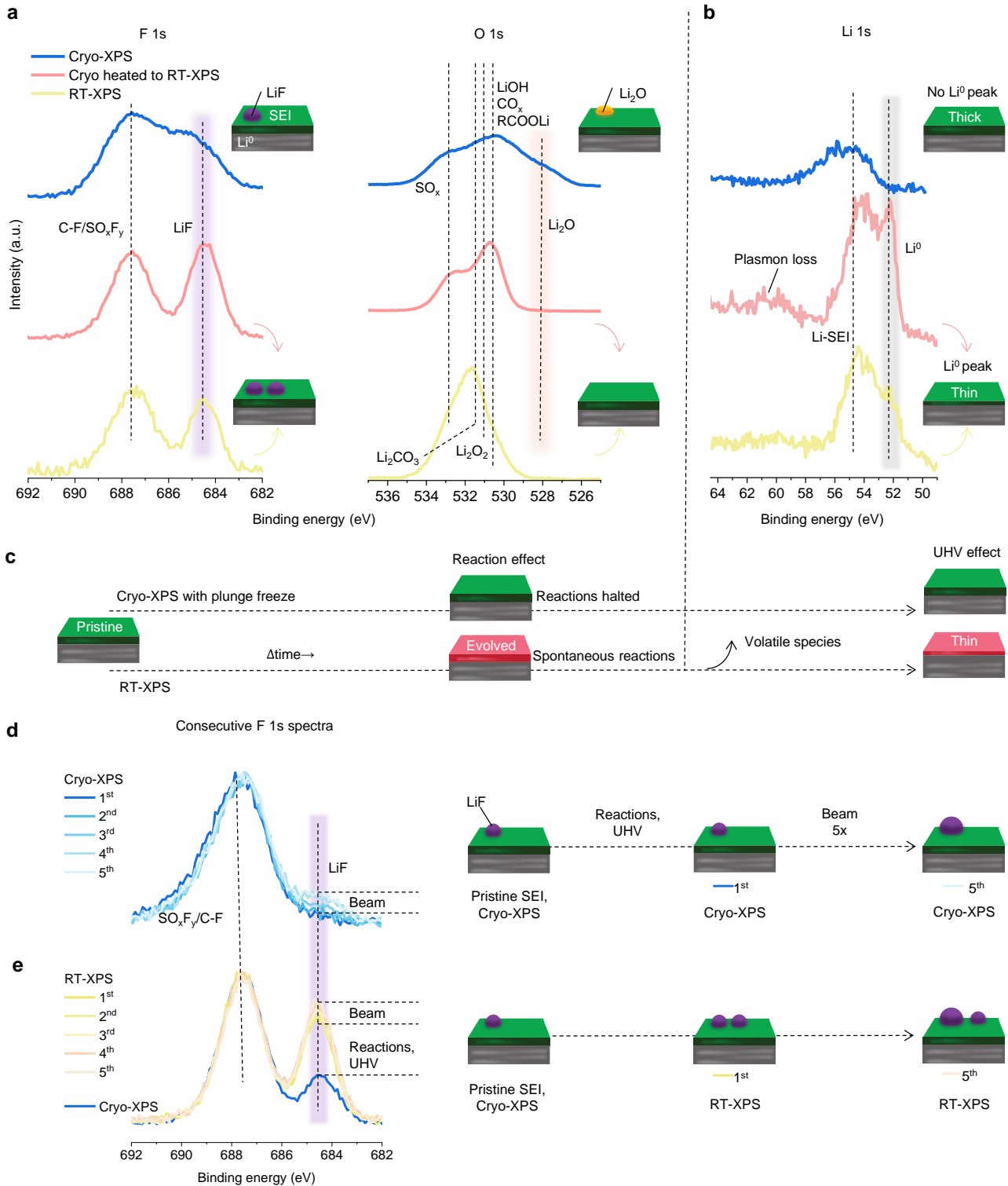


**Fig. 3. Reaction, UHV, and X-ray beam effects on SEI chemical composition.** **a-b,** High-resolution spectra for **(a)** F 1s peaks, O 1s peaks, and **(b)** Li 1s peaks collected using cryo-XPS (blue, top), cryo heated to RT-XPS (pink, middle), and RT-XPS (yellow, bottom) with schematics showing SEI evolution. **c,** Schematics showing reaction and UHV effects for cryo-XPS and RT-

XPS over time. The measurements shown in **(a)** for F 1s and O 1s are carried out using LiFSI-1.2 DME-3 TTE by molar ratio (LHCE) electrolyte. The measurements shown in **(b)** for Li 1s are carried out using 1 M LiPF<sub>6</sub>/EC-DEC (LP) electrolyte. Global normalization is performed with respect to the C-F peak in F 1s high-resolution spectra for the same electrolyte as shown in **(a)** and Extended Data Fig. 6a. **d-e**, X-ray beam effect during consecutive spectra collection. Five consecutive high-resolution spectra for F 1s peak with **(d)** cryo-XPS, **(e)** RT-XPS. The samples are compared with corresponding cryo-XPS spectra and schematics showing the effects are added. The data are normalized with respect to the C-F/SO<sub>x</sub>F<sub>y</sub> peak. The measurements are carried out using **(d)** 4 M LiFSI/DME, and **(e)** LiFSI-1.2 DME-3 TTE by molar ratio (LHCE) electrolytes. The LHCE-SEI sample is obtained from an unwashed sample. For X-ray beam effect experiments, each F 1s spectrum collection takes ~1.5 min with the set parameters.

Next, we consider the presence of a noticeable Li<sub>2</sub>O peak under cryo conditions that is absent under RT conditions in the O 1s spectral region (Fig. 3a). Because Li<sub>2</sub>O has extremely low vapor pressure and is not reported to volatilize in vacuum even at 1000 °C<sup>32,33</sup>, the absence of Li<sub>2</sub>O during RT-XPS can be justified through reaction effects (Supplementary Note 2). Interestingly, the presence of Li<sub>2</sub>O is reversed at cryoT and RT for the SEI in a low-performing carbonate electrolyte, 1 M LiPF<sub>6</sub>/EC-DEC (LP), which could be due to favorable Li<sub>2</sub>O formation reactions (Extended Data Fig. 6, Supplementary Note 2). Li<sub>2</sub>O is prevalent in the SEI from high coulombic efficiency (CE) electrolytes<sup>29</sup> and is shown to improve anodic stability<sup>30</sup>. Indeed, the Li<sub>2</sub>O content in the SEI correctly correlates with the CE trend of LHCE and carbonate electrolyte under cryo-XPS conditions. By contrast, the evolved SEI measured with RT-XPS fails to provide the relevant performance associations due to spontaneous reactions resulting in deviations from the pristine SEI.

#### *UHV effect*

We explain the UHV effect from the observation of the underlying Li<sup>0</sup> metal peak beneath the SEI. While only a broad SEI-associated Li 1s peak is observed with cryo-XPS, the metallic Li<sup>0</sup> peak appears during RT and cryo heated to RT analyses (Li 1s region, Fig. 3b). The results suggest the thinning of the SEI at RT at which the UHV effect triggers volatile species to leave the surface (Fig. 3c). The SEI thickness can be estimated from the photoelectron escape depth from Li<sup>0</sup> metal (~4.2 nm ± 20%, Supplementary Note 3)<sup>34</sup>. The observation of a Li<sup>0</sup> metal peak suggests that the SEI thickness is less than ≤4.2 nm ± 20% at RT whereas the SEI thickness is >4.2 nm ± 20% at cryoT<sup>35</sup>. This estimated SEI thickness from cryo-XPS is consistent with that from cryo-TEM measurements reported to be ≥7.7 nm for the model LP electrolyte SEI (Extended Data Fig. 7a-b)<sup>15</sup>. This result has implications for RT-XPS measurements as the SEI thickness shows a significant reduction at RT and a high deviation from the true SEI thickness. Here, a specific case of the SEI formed with LP electrolyte is shown because it displays distinguishable Li<sup>0</sup> metal peaks at RT. Further, our cryo-XPS findings compare favorably to cryo-scanning TEM electron energy loss spectroscopy (cryo-STEM EELS) data, with both demonstrating higher contribution from C=O bond from C 1s (XPS) and C K edge (EELS) respectively for LP-SEI, whereas the C=O contribution is lower for RT-XPS (Extended Data Fig. 7c-e)<sup>15</sup>.

Besides giving information on SEI thickness, Li 1s spectra can elucidate the relative diversity among different SEI species. Because most SEI species are bonded with Li, a higher full-width half maximum (FWHM) of SEI-associated Li 1s peaks can be translated to having an SEI formed by several different species bonded to Li. Contrarily, a lower FWHM suggests a more homogeneous SEI composition. A higher Li 1s FWHM is observed for LHCE-SEI at cryoT compared to RT conditions (Extended Data Fig. 8) suggesting that the SEI is more heterogeneous at its pristine state during cryo-XPS whereas only non-volatile species and stable reaction end products dominate the SEI composition at RT. This interpretation is also supported by Extended Data Fig. 9, which shows a higher degree of atomic concentration change with sputtering during cryo-XPS than cryo heated to RT-XPS, likely because both stable and unstable SEI species are preserved during cryo-XPS. In all the observed cases, the results indicate that we are only able to capture an evolved SEI with RT-XPS due to reaction and UHV effects (Fig. 3c).

### *Beam effect*

To show the beam damage effect, we collect five consecutive spectra at cryoT (Fig. 3d) and RT (Fig. 3e). The change between the consecutive spectra is a relative measure of the beam damage effect. First, we observe only a slight increase in LiF intensity after five consecutive X-ray beam exposures for both cryo-XPS and RT-XPS spectra (Fig. 3d-e). This result suggests that the composition change due to the beam damage effect is minor. Next, we assess the relative impact of beam damage decoupled from reaction and UHV effects by comparing the composition change between cryo-XPS and the 1<sup>st</sup> RT-XPS spectra (Fig. 3e). We find that the LiF intensity difference observed between cryo-XPS and the 1<sup>st</sup> RT-XPS spectra is much higher than that between the 1<sup>st</sup> and 5<sup>th</sup> RT-XPS spectra. This result indicates that the reaction and UHV effects cause major composition evolution during XPS analysis of sensitive SEI samples. Moreover, beam damage is only a minor effect during cryo-XPS causing slight composition evolution, which does not occur until the 4<sup>th</sup> consecutive spectrum (Fig. 3d). Furthermore, SEI spectra are generally not collected from the same spot multiple times in a row, so the practical spectra collection can be considered free from any significant beam damage effect. The reactions toward a slight increase in LiF content from beam damage may be due to primary photoelectron or secondary electron attack resulting in the defluorination of C-F/SO<sub>x</sub>F<sub>y</sub> species<sup>14</sup>. This observed insignificance of the X-ray beam effect in XPS is unlike TEM where electron beam damage to lithium is found to be a major effect motivating cryo-TEM<sup>12</sup>. This difference is because a low energy X-ray beam (~1.5 keV) is used in our XPS analysis whereas TEM requires a high energy electron beam (~80-300 keV) and a very thin ( $\lesssim$ 100 nm) electron transparent sample, making it more susceptible to beam damage<sup>36,37</sup>. Nonetheless, the extent of beam damage may vary based on the X-ray source and setup.

### **Correlation of pristine and evolved SEI composition with performance**

Because cryo-XPS offers information on the pristine SEI with preservation, we use it to correlate SEI composition and CE. We measure salt- and additive-derived SEI over solvent-derived SEI from XPS for different electrolyte chemistries. For LiPF<sub>6</sub> salt-based carbonate electrolytes and for LiFSI salt-based ether electrolytes, the (F + P)/C ratio and (F + S + N)/C ratio are used, respectively. The proposed ratios are rational because salt and additive-derived SEI measure the relative total inorganic or beneficial content in the SEI<sup>29,30,38-40</sup>. We calculate the Spearman

coefficient<sup>41</sup> ( $\rho$ ) to measure the strength and direction of the monotonic relationship between ranked SEI composition and CE. Although the correlation is only moderate with regular RT-XPS ( $\rho = 0.6$ , Fig. 4a), a highly positive correlation is observed with cryo-XPS ( $\rho = 0.9$ , Fig. 4b). We also study F/C and CE correlation to understand the impact of fluorinated species<sup>30,42,43</sup>. In line with the proposed benefits of fluorinated species in existing literature toward high CE<sup>27,42,44</sup>, the F/C correlation is found positive with cryo-XPS ( $\rho = 0.6$ , Extended Data Fig. 10). Counterintuitively, a negative moderate correlation is observed with RT-XPS ( $\rho = -0.6$ ), suggesting that RT-XPS is potentially ineffective in providing a rational correlation across diverse electrolyte chemistries. Moreover, we observe larger calculated ratios and larger error bars with cryo-XPS. The error bars further increase in size with additive-based LPF and LHCE. The significant deviation in the ratio values with cryo-XPS and RT-XPS is due to a combination of complex RT reactions and the UHV effect. Based on previous discussions on reaction effect (Fig. 3a) and sputtering (Extended Data Fig. 9), we speculate that only stable species dominate the composition during RT-XPS, resulting in lower heterogeneity (Fig. 4a and Extended Data Fig. 10a). By contrast, the larger error bars with cryo-XPS (Fig. 4b and Extended Data Fig. 10b) are associated with the co-existence of both stable and unstable SEI species at cryoT, resulting in a more heterogeneous composition. The higher heterogeneity of the pristine SEI composition found with cryo-XPS can be further rationalized knowing that the SEI is inherently heterogeneous<sup>4,5,45</sup>. The results overall indicate that cryo-XPS provides improved and rational performance-based correlations across different electrolyte chemistries.

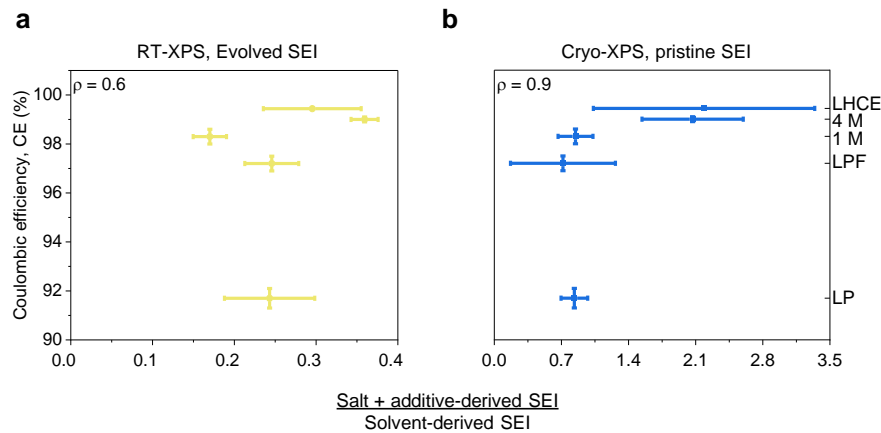


**Fig. 4. Correlation between relative salt and additive-derived SEI content and CE across diverse electrolyte chemistries.** **a-b**, CE (Supplementary Table 1) from Aubach's method<sup>15,46</sup> in relation to relative salt and fluorinated additive-derived content of SEI from (a) RT-XPS and (b) cryo-XPS. (Salt + additive-derived SEI)/Solvent-derived SEI indicates  $(F + S + N)/C$  in LiFSI-based and  $(F + P)/C$  in LiPF<sub>6</sub>-based electrolytes. The measurements are carried out in 1 M LiPF<sub>6</sub>/EC-DEC (LP), 90 vol% 1 M LiPF<sub>6</sub>/EC-DEC with 10 vol% FEC (LPF), 1 M LiFSI/DME (1M), 4 M LiFSI/DME (4M), and LiFSI-1.2 DME-3 TTE by molar ratio (LHCE) electrolytes. The error bars of XPS results are calculated from the analysis of three different spots of the same sample. Spearman rank correlation coefficient<sup>41</sup> ( $\rho$ ) is calculated from the average values of the CE and relative salt and additive-derived content.

Our description of the pristine SEI from cryo-XPS avoids previous limitations of irreversible chemical compositional evolution of the SEI and volatilization of species under UHV. Moreover,

from the pristine SEI chemical composition obtained through cryo-XPS, we find a significant positive correlation between the inorganic-rich SEI content and CE across different electrolyte classes. While our results challenge existing analyses of the SEI based on characterization with RT-XPS, we view this as an opportunity to redefine our understanding and provide a more reliable interpretation of the pristine SEI speciation. By providing a more precise chemical understanding of the SEI in its pristine form, we anticipate our study will accelerate the achievement of commercially viable Li metal batteries. Most importantly, we expect our research to inspire future studies of sensitive and reactive interface characterization under cryogenic conditions to ensure pristine state preservation.

## Methods

### *Materials*

All electrolytes were prepared and handled in an argon-filled glovebox with an O<sub>2</sub> concentration of <0.1 ppm and H<sub>2</sub>O concentration of <0.01 ppm. Lithium bis(fluorosulfonyl)imide or LiFSI (Fluolyte) was used as a salt. 1,2-dimethoxyethane or DME (Sigma-Aldrich) and DEC (Sigma-Aldrich) were used as solvents. 1,1,2,2-tetrafluoroethyl 2,2,3,3-tetrafluoropropylether or TTE (SynQuest) was used as a diluent in LHCE electrolyte. 1 M lithium hexafluorophosphate or LiPF<sub>6</sub> in EC/DEC (LP) and fluoroethylene carbonate or FEC were purchased from Gotion. The electrolyte formulations used were 1 M LiPF<sub>6</sub>/EC-DEC (LP), 90 vol% 1 M LiPF<sub>6</sub>/EC-DEC with 10 vol% FEC (LPF), 1 M LiFSI/DME (1M), 4 M LiFSI/DME (4M), and LiFSI-1.2 DME-3 TTE by molar ratio (LHCE) (Supplementary Table 1). The commercial Li battery separator Celgard 2325 (25 µm thick, polypropylene/polyethylene/polypropylene or PP/PE/PP was purchased from Celgard. CR2032-type coin cells were used for all experiments. Thick Li foil (~750 µm thick) and Cu current collector (25 µm thick Cu foil) were purchased from Alfa Aesar.

### *Electrochemical measurement*

All electrochemical measurements were performed using an Arbin battery cycler with Li|Cu coin cells. All cells were made inside an argon-filled glovebox. Li was mechanically scraped with a polyethylene scraper to remove the surface oxide and improve the electrical connection. 60 µL of electrolytes were used in all the coin cells. The coin cells were transferred inside the glovebox for sample preparation immediately after the electrochemical tests. For SEI characterization on top of electrodeposited lithium, a plating capacity of 0.5 mAh cm<sup>-2</sup> and a current density of 1 mA cm<sup>-2</sup> were used for all XPS experiments. For SEI characterization on top of the Cu current collector prior to Li electrodeposition (Extended Data Fig. 5), a 10 mV vs. Li/Li<sup>+</sup> potential hold was applied on Cu for 30 min.

### *Materials Characterization*

The cryo-XPS transfer protocol is shown in Fig. 1. The Versa Probe IV XPS instrument (PHI, Inc.) available at Stanford Nano Shared Facilities was used for all the XPS experiments. Unless otherwise mentioned, 60 µL of respective solvent (DEC for LP and LPF, and DME for 1M, 4M, and LHCE) was used after cell disassembly for rinsing the electroplated Li<sup>0</sup> on Cu current collector. A manual hand blower was used for drying the SEI quickly (~4-8 s) inside the glovebox. A quick drying process was chosen so that the sample could be frozen and the spontaneous room

temperature reactions could be halted as soon as possible. For the specific cases of unwashed SEI, the sample was kept unwashed and ~3-5 s of manual one-sided blotting was performed using a filter paper (Whatman™ 42.5mm Ø) and tweezer adapted from<sup>15</sup> to remove excess electrolyte. The drying time and blotting time slightly varied for different electrolytes and the best human judgment was used to ensure completion (no visible signs of liquid or wetness). The Cu current collector was cut in half to reduce pumping time. The samples were then put inside a sealed Eppendorf tube and taken out from the glovebox to immediately plunge freeze by breaking the tube with pliers in liquid N<sub>2</sub> (~−196 °C) without any air exposure. Then, the samples were transferred to XPS using a larger liquid N<sub>2</sub> dewar that contained the cryogenic sample storage vial. The cryo-XPS sample holder was precooled to -110 °C (minimum allowed temperature) before loading the cryogenic samples in the intro chamber to maintain the cryo conditions of the sample. The cryogenic sample holder was a specialized sample holder with a cold finger connected through stage control for *in situ* cooling. The N<sub>2</sub> pressure, higher than ambient pressure, inside the intro chamber ensured an inert environment around the sample to preserve it from air and moisture right before pumping. Due to the fast-pumping process of the instrument (~5-10 min) and the precooled sample holder, the samples maintained cryoT. Approximately 10 min of pumping results in a sample temperature of ~−110 °C as estimated from the reading of a thermocouple placed on the holder in the main chamber. A continuous supply of liquid N<sub>2</sub> was provided to the cold finger, and a PID controller was used to maintain a temperature of ~−110 °C in the main chamber. The spectral collection was also performed at ~−110 °C during cryo-XPS.

For cryo heated to RT-XPS (~25 °C), the PID controller set parameters were optimized to prevent any sudden temperature spikes above room temperature, and the same parameters were used for all the samples to ensure a comparable heating rate. Please refer to Supplementary Table 2 for the values of PID controller parameters. The heating process took ~8.5 min from -110 °C to 25 °C (set point). For RT-XPS, after sample preparation, the samples were transferred from the argon-filled glovebox to the XPS chamber using a sealed vessel, and experiments were performed using regular sample holders.

The XPS measurements performed in the Versa Probe IV XPS instrument (PHI, Inc.) utilizes a monochromatic Al-K source at 1486.6 eV. In the built-in conditions of the instrument, the angle between the analyzer and sample holder is 45°, which was used during all the experiments. Please read Supplementary Note 3 for further details on photoelectron escape depth. A precise z-height calibration was ensured before spectra collection to maximize the photoelectron signal. High resolution scans were collected using a 55 eV pass energy, 0.81 eV energy resolution, 20 ms dwell time, and step size of 0.1 eV. Survey scans were collected using a 224 eV pass energy, 1.40 eV energy resolution, 20 ms dwell time, and 0.8 eV step size. For Ar<sup>+</sup> sputtering, a 1 kV, 0.7 μA, 22 mm gun setting was used for 30 s at an angle of 33° to the sample holder. Due to the poor electrical conductivity of the SEI, electron and ion neutralizers were used during spectra collection. Please refer to Baer *et al.*<sup>47</sup> for more details about using charge neutralization and Zhang *et al.*<sup>15</sup> for cryo-TEM and cryo-STEM EELS measurements and sample preparation.

All XPS data were analyzed using the Multipak software (PHI, Inc.). We used LiF-based<sup>8</sup> spectral calibration as C 1s-based calibration may lead to misinterpretations<sup>48</sup>. The LiF peak position was fixed at 684.5 eV, consistent with the literature<sup>49,50</sup>. For every spectrum, the relative positions of all the peaks were checked to ensure the calibration was correct. Peaks were assigned based on

several articles<sup>7,30,42,51–53</sup> with the best human judgement, and LiF-based relative shifting was applied to the referenced articles to ensure peak position accuracy.

## References

1. Bard, A. J. *et al.* The Electrode/Electrolyte Interface-A Status Report. *J Phys Chem* **97**, 7147–7173 (1993).
2. Yu, X. & Manthiram, A. Electrode-electrolyte interfaces in lithium-based batteries. *Energy Environ Sci* **11**, 527–543 (2018).
3. Stamenkovic, V. R., Strmcnik, D., Lopes, P. P. & Markovic, N. M. Energy and fuels from electrochemical interfaces. *Nat Mater* **16**, 57–69 (2016).
4. Lin, D., Liu, Y. & Cui, Y. Reviving the lithium metal anode for high-energy batteries. *Nat Nanotechnol* **12**, 194–206 (2017).
5. Li, Y., Leung, K. & Qi, Y. Computational Exploration of the Li-Electrode|Electrolyte Interface in the Presence of a Nanometer Thick Solid-Electrolyte Interphase Layer. *Acc Chem Res* **49**, 2363–2370 (2016).
6. Winter, M. The Solid Electrolyte Interphase-The Most Important and the Least Understood Solid Electrolyte in Rechargeable Li Batteries. *Z. Phys. Chem* **223**, 1395–1406 (2009).
7. Oyakhire, S. T., Gong, H., Cui, Y., Bao, Z. & Bent, S. F. An X-ray Photoelectron Spectroscopy Primer for Solid Electrolyte Interphase Characterization in Lithium Metal Anodes. *ACS Energy Lett* **7**, 2540–2546 (2022).
8. Yu, W., Yu, Z., Cui, Y. & Bao, Z. Degradation and Speciation of Li Salts during XPS Analysis for Battery Research. *ACS Energy Lett* **7**, 3270–3275 (2022).
9. Dedryvère, R. *et al.* XPS Identification of the Organic and Inorganic Components of the Electrode/Electrolyte Interface Formed on a Metallic Cathode. *J Electrochem Soc* **152**, A689 (2005).
10. Kanamura, K., Tamura, H., Shiraishi, S. & Takehara, Z.-I. XPS Analysis for the Lithium Surface Immersed in γ-butyrolactone Containing Various Salts. *J Electrochem Soc* **40**, 913–921 (1995).
11. Andersson, A. M. & Edström, K. Chemical Composition and Morphology of the Elevated Temperature SEI on Graphite. *J Electrochem Soc* **148**, A1100 (2001).
12. Li, Y. *et al.* Atomic structure of sensitive battery materials and interfaces revealed by cryo-electron microscopy. *Science* **358**, 27 (2017).
13. Boyle, D. T. *et al.* Corrosion of lithium metal anodes during calendar ageing and its microscopic origins. *Nat Energy* **6**, 487–494 (2021).
14. Steinrück, H. G. *et al.* Interfacial Speciation Determines Interfacial Chemistry: X-ray-Induced Lithium Fluoride Formation from Water-in-salt Electrolytes on Solid Surfaces. *Angewandte Chemie - International Edition* **59**, 23180–23187 (2020).
15. Zhang, Z. *et al.* Capturing the swelling of solid-electrolyte interphase in lithium metal batteries. *Science* **375**, 66–70 (2022).

16. Wang, X. *et al.* New Insights on the Structure of Electrochemically Deposited Lithium Metal and Its Solid Electrolyte Interphases via Cryogenic TEM. *Nano Lett* **17**, 7606–7612 (2017).
17. Zachman, M. J., Tu, Z., Choudhury, S., Archer, L. A. & Kourkoutis, L. F. Cryo-STEM mapping of solid–liquid interfaces and dendrites in lithium-metal batteries. *Nature* **560**, 345–349 (2018).
18. Zhang, Z. *et al.* Cryogenic Electron Microscopy for Energy Materials. *Acc Chem Res* **54**, 3505–3517 (2021).
19. Bai, X. chen, McMullan, G. & Scheres, S. H. W. How cryo-EM is revolutionizing structural biology. *Trends Biochem Sci* **40**, 49–57 (2015).
20. Dubochet, J. On the Development of Electron Cryo-Microscopy (Nobel Lecture). *Angewandte Chemie* **130**, 11008–11013 (2018).
21. Henderson, R. From Electron Crystallography to Single Particle CryoEM (Nobel Lecture). *Angewandte Chemie* **130**, 10966–10989 (2018).
22. Taylor, K. A. & Glaeser, R. M. Electron Diffraction of Frozen, Hydrated Protein Crystals. *Science* **186**, 1036–1037 (1974).
23. McDowall, A. W. *et al.* Electron microscopy of frozen hydrated sections of vitreous ice and vitrified biological samples. *J Microsc* **131**, 1–9 (1983).
24. Henderson, R., Baldwin, J. M., Downing, K. H., Lepault, J. & Zemlin, F. Structure of Purple Membrane From Halobacterium Halobium: Recording, Measurement and Evaluation of Electron Micrographs at 3.5 Å Resolution. *Ultramicroscopy* **19**, 147–178 (1986).
25. Fernandez-Moran, H. Cell-Membrane Ultrastructure Low-Temperature Electron Microscopy and X-Ray Diffraction Studies of Lipoprotein Components in Lamellar Systems. *Circulation* **26**, 1039–1065 (1962).
26. Tan, J., Matz, J., Dong, P., Shen, J. & Ye, M. A Growing Appreciation for the Role of LiF in the Solid Electrolyte Interphase. *Adv Energy Mater* **11**, (2021).
27. Li, T., Zhang, X. Q., Shi, P. & Zhang, Q. Fluorinated Solid-Electrolyte Interphase in High-Voltage Lithium Metal Batteries. *Joule* **3**, 2647–2661 (2019).
28. Wang, C., Meng, Y. S. & Xu, K. Perspective—Fluorinating Interphases. *J Electrochem Soc* **166**, A5184–A5186 (2019).
29. Hobold, G. M., Wang, C., Steinberg, K., Li, Y. & Gallant, B. M. High lithium oxide prevalence in the lithium solid–electrolyte interphase for high Coulombic efficiency. *Nat Energy* **9**, 580–591 (2024).
30. Kim, M. S. *et al.* Suspension electrolyte with modified Li<sup>+</sup> solvation environment for lithium metal batteries. *Nat Mater* **21**, 445–454 (2022).
31. Lin, D. *et al.* Fast galvanic lithium corrosion involving a Kirkendall-type mechanism. *Nat Chem* **11**, 382–389 (2019).
32. Arkel, A. E., Spitsbergen, U. & Heyding, R. D. Note on the volatility of lithium oxide. *Can J Chem* **33**, 446–447 (1955).

33. Kudo, H., Wu, C. H. & Ihle, H. R. Mass-spectrometric study of the vaporization of Li<sub>2</sub>O(s) and thermochemistry of gaseous LiO, Li<sub>2</sub>O, Li<sub>3</sub>O, and Li<sub>2</sub>O<sub>2</sub>. *Journal of Nuclear Materials* **78**, 380–389 (1978).
34. Seah, M. P. & Dench, W. A. Quantitative electron spectroscopy of surfaces: A standard data base for electron inelastic mean free paths in solids. *Surface and Interface Analysis* **1**, 2–11 (1979).
35. D'Acunto, G. *et al.* Atomic Layer Deposition of Hafnium Oxide on InAs: Insight from Time-Resolved in Situ Studies. *ACS Appl Electron Mater* **2**, 3915–3922 (2020).
36. Walther, T. Transmission Electron Microscopy of Nanostructures. in *Microscopy Methods in Nanomaterials Characterization* 105–134 (Elsevier, 2017). doi:10.1016/B978-0-323-46141-2.00004-3.
37. García De Abajo, F. J. & Di Giulio, V. Optical Excitations with Electron Beams: Challenges and Opportunities. *ACS Photonics* **8**, 945–974 (2021).
38. Jagger, B. & Pasta, M. Solid electrolyte interphases in lithium metal batteries. *Joule* **7**, 2228–2244 (2023).
39. He, M., Guo, R., Hobold, G. M., Gao, H. & Gallant, B. M. The intrinsic behavior of lithium fluoride in solid electrolyte interphases on lithium. doi:10.1073/pnas.1911017116/-/DCSupplemental.
40. Kim, M. S. *et al.* Revealing the Multifunctions of Li<sub>3</sub>N in the Suspension Electrolyte for Lithium Metal Batteries. *ACS Nano* **17**, 3168–3180 (2023).
41. Spearman, C. The Proof and Measurement of Association between Two Things. *Source: The American Journal of Psychology* **15**, 72–101 (1904).
42. Oyakhire, S. T. *et al.* Proximity Matters: Interfacial Solvation Dictates Solid Electrolyte Interphase Composition. *Nano Lett* **23**, 7524–7531 (2023).
43. Oyakhire, S. T. & Bent, S. F. Interfacial engineering of lithium metal anodes: what is left to uncover? *Energy Advances* **3**, 108–122 (2023).
44. Yu, Z. *et al.* Rational solvent molecule tuning for high-performance lithium metal battery electrolytes. *Nat Energy* **7**, 94–106 (2022).
45. Peled, E. & Ardel, G. Advanced Model for Solid Electrolyte Interphase Electrodes in Liquid and Polymer Electrolytes. *J Electrochem Soc* **144**, L208 (1997).
46. Cui, Z. *et al.* Molecular anchoring of free solvents for high-voltage and high-safety lithium metal batteries. *Nat Commun* **15**, (2024).
47. Baer, D. R. *et al.* XPS guide: Charge neutralization and binding energy referencing for insulating samples. *Journal of Vacuum Science & Technology A* **38**, (2020).
48. Greczynski, G. & Hultman, L. Compromising Science by Ignorant Instrument Calibration—Need to Revisit Half a Century of Published XPS Data. *Angewandte Chemie - International Edition* **59**, 5002–5006 (2020).
49. Liu, Q. *et al.* A fluorinated cation introduces new interphasial chemistries to enable high-voltage lithium metal batteries. *Nat Commun* **14**, (2023).

50. Ge, S. *et al.* High safety and cycling stability of ultrahigh energy lithium ion batteries. *Cell Rep Phys Sci* **2**, (2021).
51. Wood, K. N. & Teeter, G. XPS on Li-Battery-Related Compounds: Analysis of Inorganic SEI Phases and a Methodology for Charge Correction. *ACS Appl Energy Mater* **1**, 4493–4504 (2018).
52. Rustomji, C. S. *et al.* Liquefied gas electrolytes for electrochemical energy storage devices. *Science* **356**, (2017).
53. Ren, X. *et al.* Enabling High-Voltage Lithium-Metal Batteries under Practical Conditions. *Joule* **3**, 1662–1676 (2019).
54. Greczynski, G. & Hultman, L. Towards reliable X-ray photoelectron spectroscopy: Sputter-damage effects in transition metal borides, carbides, nitrides, and oxides. *Appl Surf Sci* **542**, (2021).

## Acknowledgments

S.B.S acknowledges support from the TomKat Center Graduate Fellowship for Translational Research and the Link Foundation Energy Fellowship. G.D.A. acknowledges support from the Wallenberg Foundation Postdoctoral Scholarship Program. S.T.O. acknowledges support from the Schmidt Science Postdoctoral Fellowship. K.M.S.G. acknowledges support from NSF GRFP. Y.C. acknowledges the CryoEM research support from the Department of Energy, Office of Basic Energy Sciences, Division of Materials Science and Engineering under contract DE-AC02-76SF00515, and the support from Assistant Secretary for Energy Efficiency and Renewable Energy, Office of Vehicle Technologies, of the U.S. Department of Energy under the Battery Materials Research (BMR) Program, the Battery500 Consortium program, and the CEI consortium program. S.F.B. acknowledges support from the Stanford StorageX initiative seed grant award. Part of this work was performed at the Stanford Nano Shared Facilities (SNSF) supported by National Science Foundation under the award ECCS-2026822. S.B.S. gratefully acknowledges helpful discussions with Jane Lee and Wenbo Zhang about cryo-XPS transfer. S.B.S. sincerely appreciates Donglin Li and Jun Ho Lee for providing the LHCE electrolyte.

## Author contributions

S.B.S., S.F.B., and Y.C. conceived the idea and designed experiments. S.B.S. performed all the electrochemical experiments and conducted all the RT-XPS and cryo-XPS experiments. S.B.S. and G.D.A. developed the cryo-XPS transfer process. G.D.A. assisted in cryo-XPS experiments during the initial phase. P.S. and S.T.O. assisted with experiment designs. J.R.-J. helped with cryo-XPS transfer development and instrument-related discussions. S.B.S. analyzed and interpreted the data with assistance and feedback from all the authors. S.B.S. wrote the first draft of the manuscript, which was edited and revised by all the authors. S.F.B. and Y.C. supervised the project in all aspects.

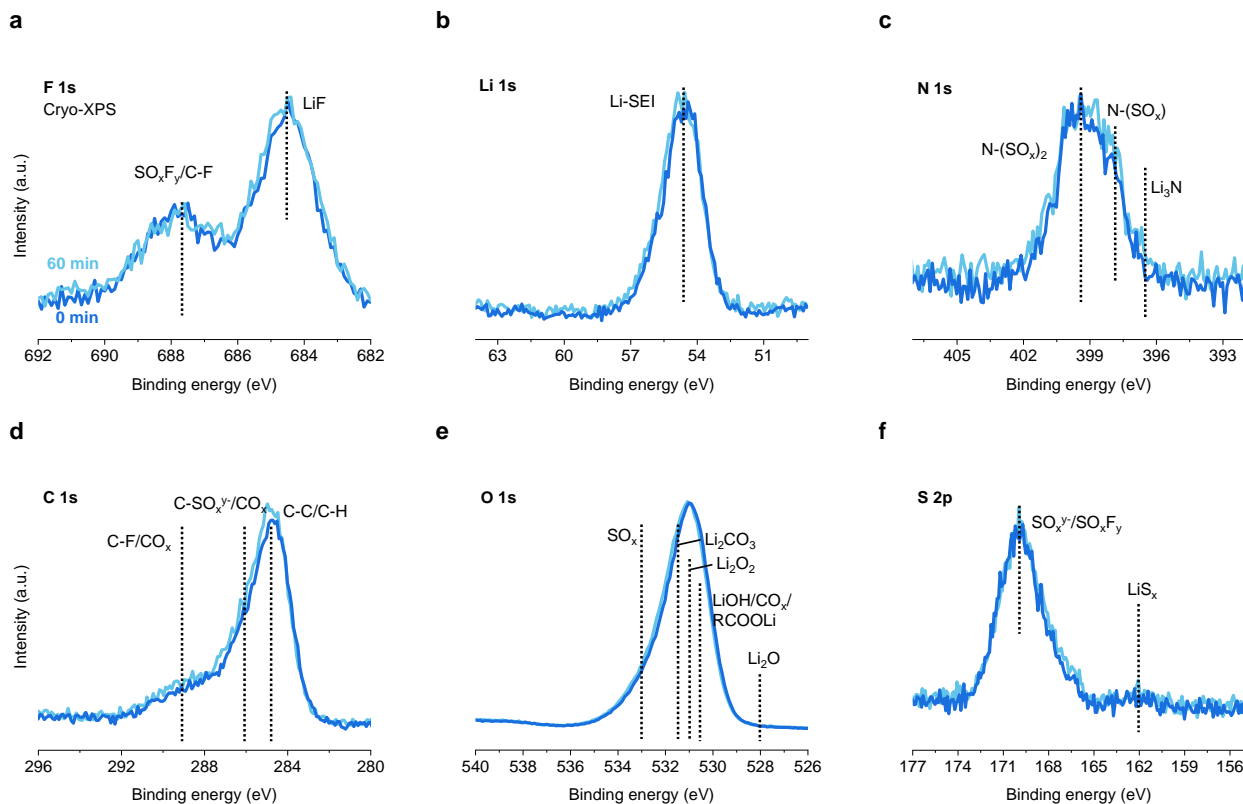
## Competing interests

The authors declare that they have no competing interests.

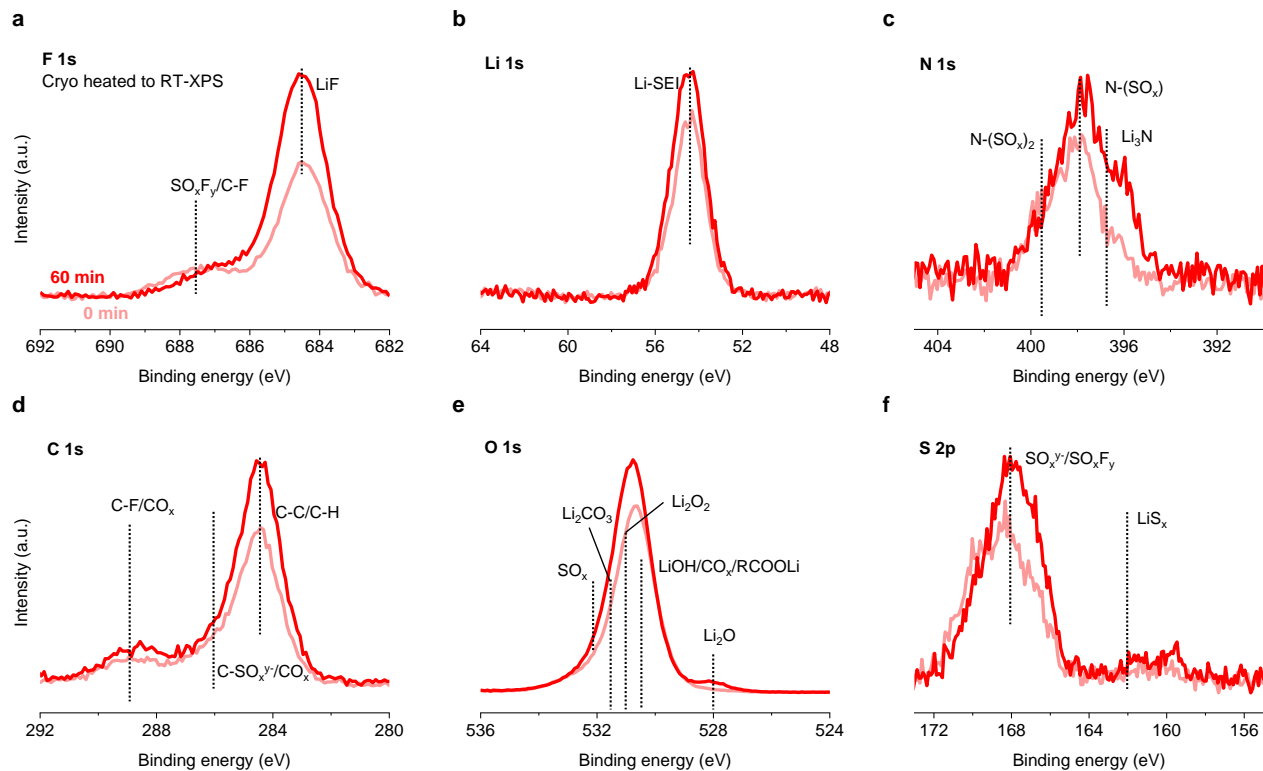
## Data availability

All data needed to evaluate the conclusions are present in the article or the supplementary materials.

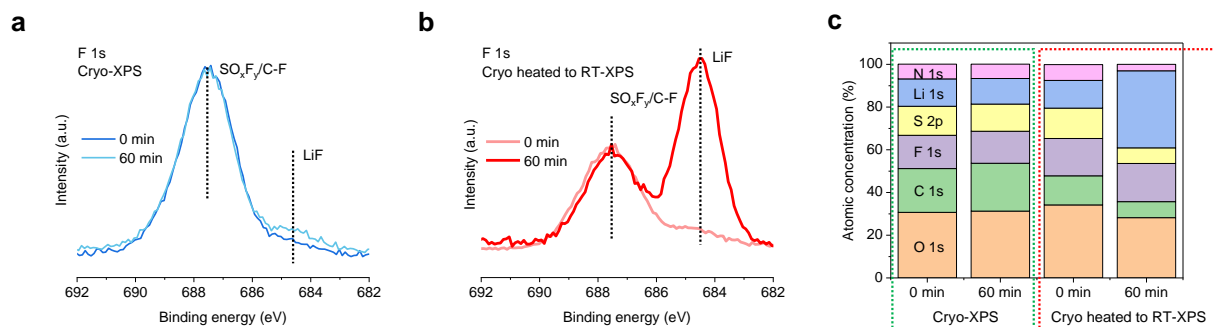
## Extended Data



**Extended Data Fig. 1.** Time-resolved high-resolution spectra for SEI with cryo-XPS. **a-f**, All high-resolution spectra for **(a)** F 1s, **(b)** Li 1s, **(c)** N 1s, **(d)** C 1s, **(e)** O 1s, **(f)** S 2p with cryo-XPS at 0 min and 60 min. The measurements are carried out in 1 M LiFSI/DME (1M) electrolyte. Global normalization of all the peaks is performed with respect to the C-F/SO<sub>x</sub>F<sub>y</sub> peak in F 1s high-resolution spectra in **(a)**. The measurements are performed on one analysis spot to capture the SEI evolution decoupled from spatial heterogeneities in the SEI.

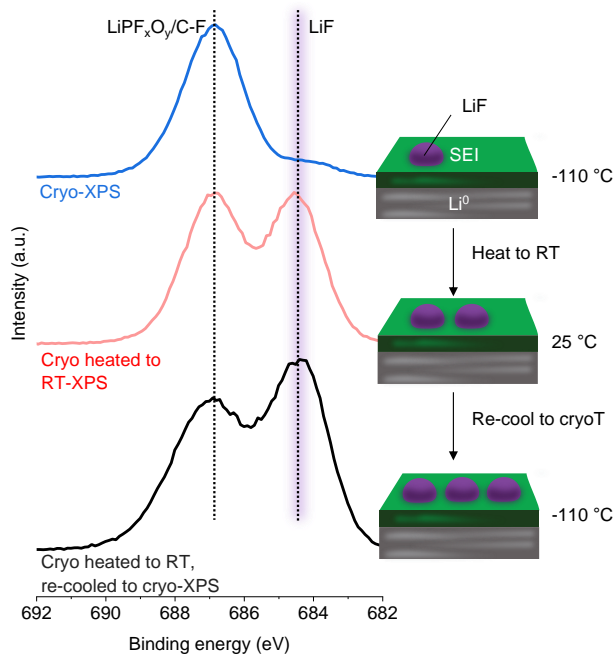


**Extended Data Fig. 2.** Time-resolved high-resolution spectra for SEI during cryo heated to RT-XPS. **a-f**, All high-resolution spectra for **(a)** F 1s, **(b)** Li 1s, **(c)** N 1s, **(d)** C 1s, **(e)** O 1s, **(f)** S 2p with cryo heated to RT-XPS at 0 min and 60 min. The measurements are carried out in 1 M LiFSI/DME (1M) electrolyte. Global normalization of all the peaks is performed with respect to the C-F peak in F 1s high-resolution spectra in **(a)**. The measurements are performed on one analysis spot to capture the SEI evolution decoupled from spatial heterogeneities in the SEI. The analysis spot is the same as the one shown in Extended Data Fig. 1.

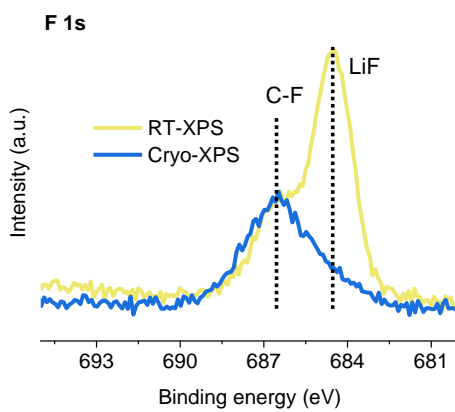


**Extended Data Fig. 3.** SEI preservation and evolution effects with cryo-XPS and RT-XPS on unwashed SEI. **a-b**, High-resolution spectra for F 1s peaks with **(a)** cryo-XPS and **(b)** cryo heated to RT-XPS at 0 min and at 60 min. **c**, Atomic concentration for unwashed SEI with cryo-XPS and cryo heated to RT-XPS at 0 min and at 60 min. The intensities of F 1s spectra shown in **(a)** and **(b)** are normalized with respect to the SO<sub>x</sub>F<sub>y</sub>/ C-F peak. The measurements are performed on one

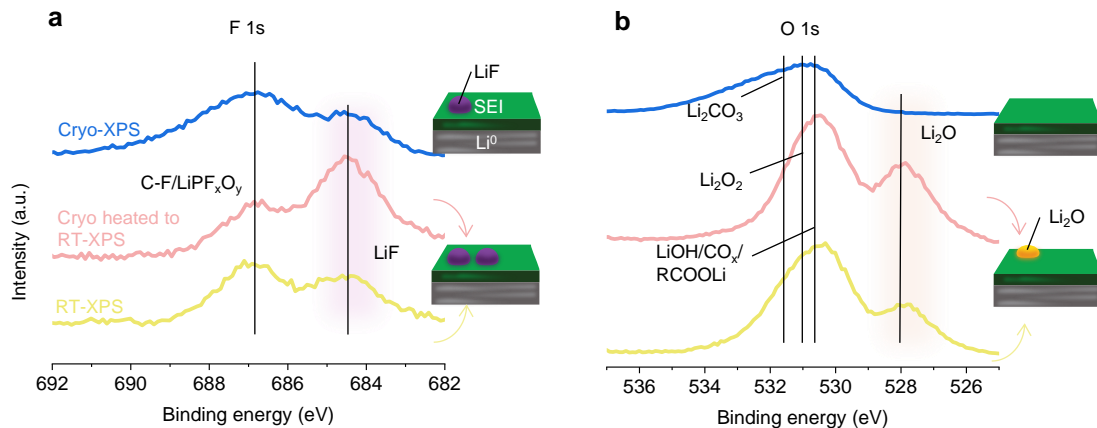
analysis spot to capture the SEI evolution decoupled from spatial heterogeneities in the SEI. The measurements are carried out in 1 M LiFSI/DME (1M) electrolyte.



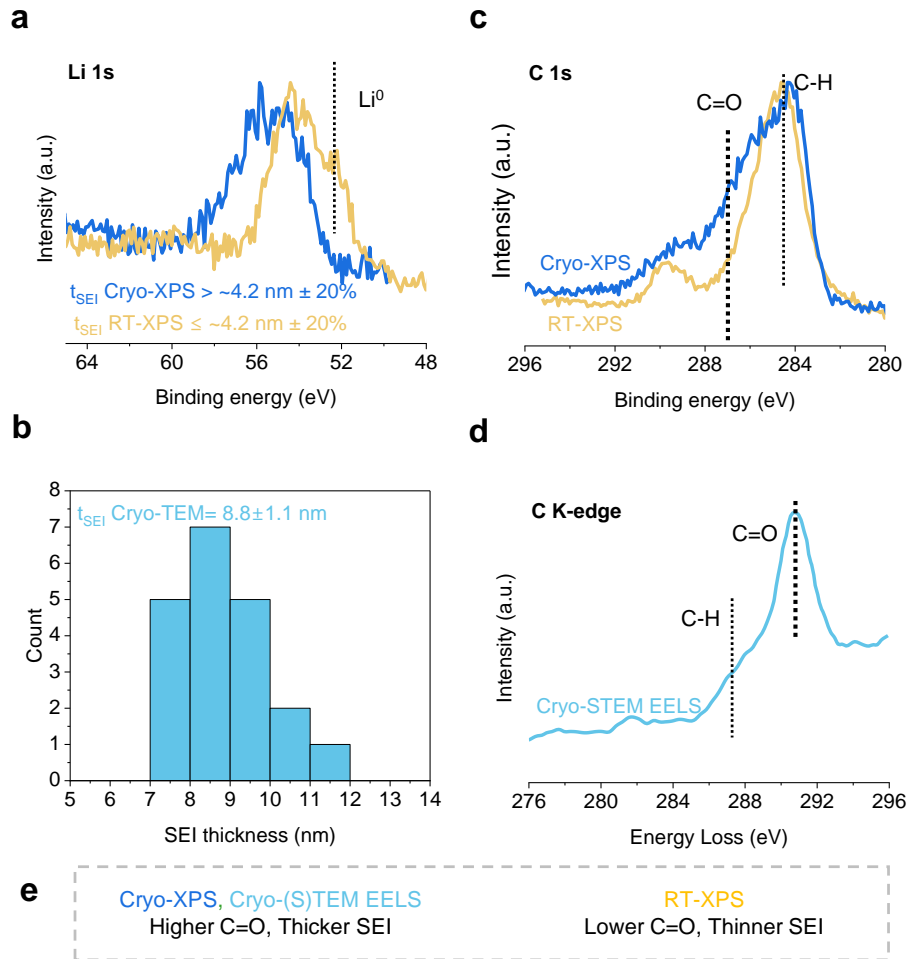
**Extended Data Fig. 4.** Effect of gradual re-cooling on SEI preservation. High-resolution F 1s spectra for with cryo-XPS (blue, top), cryo-heated to RT-XPS (pink, middle), cryo-heated to RT, and then re-cooled to cryo-XPS (black, bottom), respectively. The measurements are performed on one analysis spot to capture the SEI evolution decoupled from spatial heterogeneities in the SEI. The measurements are carried out in 1 M LiPF<sub>6</sub>/EC-DEC (LP) electrolyte. An unwashed SEI sample is used as the composition is found to be more sensitive to temperature change in Extended Data Fig. 3.



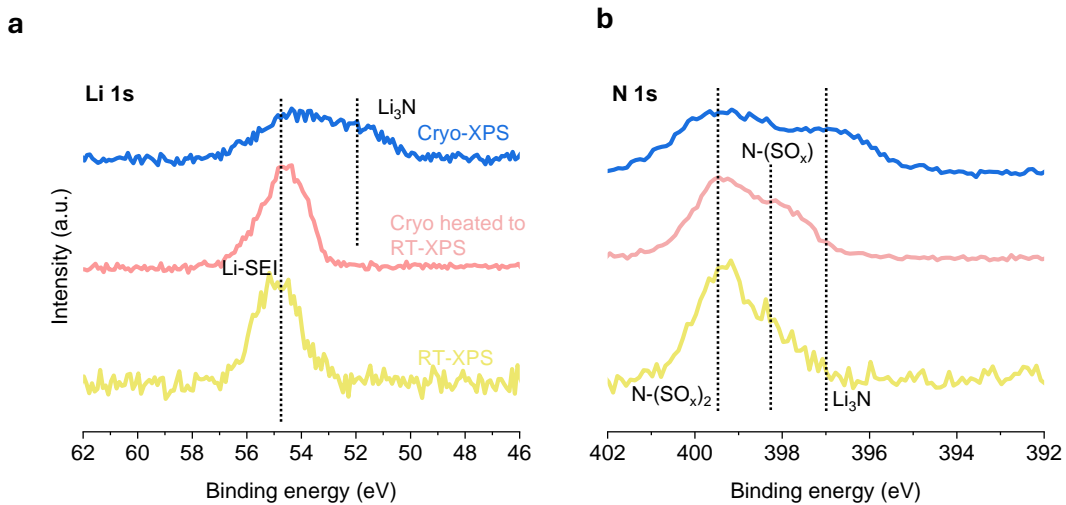
**Extended Data Fig. 5.** Effect of cryo-XPS and RT-XPS on the SEI formed on Cu before Li plating. High-resolution spectra for F 1s peaks of SEI formed on Cu in 1 M LiPF<sub>6</sub>/EC-DEC (LP) electrolyte using a protocol of holding the Cu current collector at 10 mV above Li electrodeposition potential for 30 min using cryo-XPS and RT-XPS. This protocol ensures no Li is electrodeposited on Cu so that only electrolyte decomposition prior to Li plating can be studied.



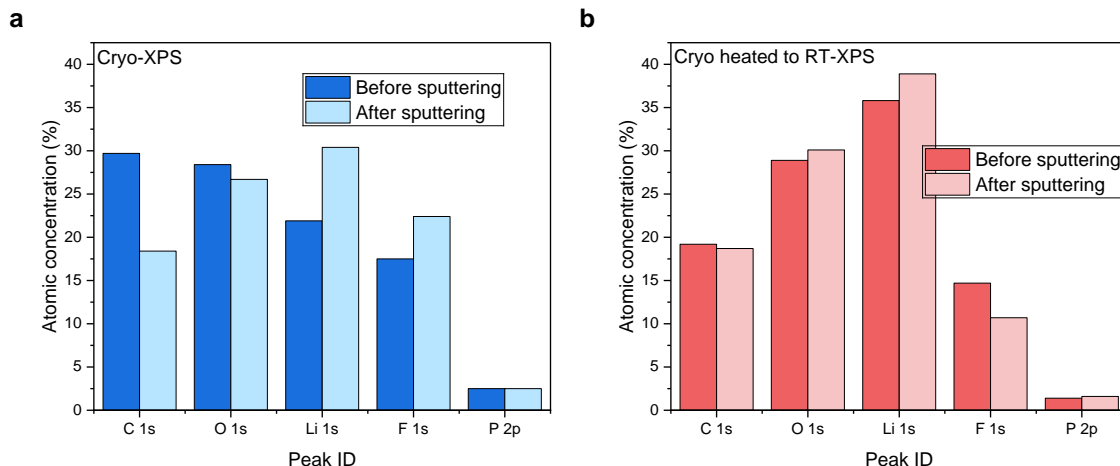
**Extended Data Fig. 6.** Reaction effect on SEI chemical composition under cryo-XPS and RT-XPS conditions. **a-b**, High-resolution spectra for **(a)** F 1s peaks and **(b)** O 1s peaks collected using cryo-XPS (blue, top), cryo heated to RT-XPS (pink, middle), and RT-XPS (yellow, bottom) with schematics showing SEI evolution. Global normalization across F 1s and O 1s is performed for the same electrolyte with respect to the C-F peak in F 1s high-resolution spectra shown in **(a)**. The measurements are carried out in 1 M LiPF<sub>6</sub>/EC-DEC (LP) electrolyte.



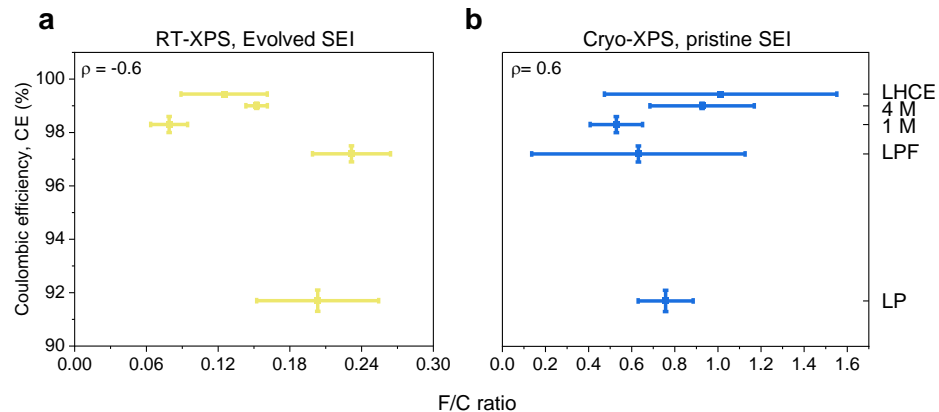
**Extended Data Fig. 7.** Cryo-XPS and RT-XPS comparison with cryo-(S)TEM EELS findings. **a**, **c**, High-resolution spectra for **(a)** Li 1s peaks and **(c)** C 1s peaks with cryo-XPS and RT-XPS. **b**, Histogram showing thickness distribution of the SEI using cryo-TEM. **d**, C K-edge fine structure of Li dendrites using cryo-STEM EELS. **e**, Summary of key findings from cryo-XPS, cryo-STEM EELS and RT-XPS. The intensities of C 1s and Li 1s spectra shown in **(a)** and **(c)** are normalized to exhibit the same maximum intensity for both cryo-XPS and RT-XPS data. The measurements in **(a)-(d)** are carried out on **(a), (c)** 0.5 mAh cm<sup>-2</sup> and **(b), (d)** 0.1 mAh cm<sup>-2</sup> Li deposited on **(a), (c)** Cu foil and **(b), (d)** Cu-evaporated TEM grid at a current density of 1 mA cm<sup>-2</sup> in 1 M LiPF<sub>6</sub>/EC-DEC (LP) electrolyte and rinsed by 60 µL DEC.  $t_{SEI}$  refers to thickness of the SEI. The data shown in **(b)** and **(d)** are extracted from literature<sup>14</sup>.



**Extended Data Fig. 8.** Temperature-dependent composition evolution effects on SEI species with cryo-XPS and RT-XPS in LHCE-SEI. **a-b**, High-resolution spectra for (a) Li 1s and (b) N 1s peaks with cryo-XPS (blue, top), cryo heated to RT-XPS (pink, middle), and RT-XPS (yellow, bottom). Global normalization is performed with respect to the C-F peak in F 1s high-resolution spectra shown in Fig. 3a. The measurements are carried out in LiFSI-1.2 DME-3 TTE by molar ratio (LHCE) electrolyte. We identify the peak near ~52 eV with cryo-XPS as Li<sub>3</sub>N (not Li<sup>0</sup> metal) because it appears and disappears in conjunction with the same species peak in N 1s region. Besides, Li is highly electropositive, so it is more favorable for Li to exist in its compound forms.



**Extended Data Fig. 9.** Effect of Ar<sup>+</sup> ion sputtering on SEI composition during cryo-XPS and RT-XPS. **a-b**, SEI composition before and after Ar<sup>+</sup> ion sputtering with (a) cryo-XPS and (b) cryo-heated to RT-XPS. The measurements in (a) and (b) are performed on different analysis spots. The measurements are carried out in an unwashed SEI sample using 1 M LiPF<sub>6</sub>/EC-DEC (LP) electrolyte. Ar<sup>+</sup> ion sputtering is destructive toward surface chemical composition<sup>7,8,54</sup>. So, the degree of composition change before and after Ar<sup>+</sup> ion sputtering is used to approximate the relative amount of stable species in the SEI.



**Extended Data Fig. 10. a-b,** Correlation between F/C ratio and CE in multiple electrolytes with cryo-XPS and RT-XPS. CE (Supplementary Table 1) from Aubach's method<sup>15,46</sup> in relation to the F/C ratio of SEI from (a) RT-XPS and (b) cryo-XPS. The measurements are carried out on 0.5 mAh cm<sup>-2</sup> of Li deposited on Cu at a current density of 1 mA cm<sup>-2</sup> in 1 M LiPF<sub>6</sub>/EC-DEC (LP), 90 vol% 1 M LiPF<sub>6</sub>/EC-DEC with 10 vol% FEC (LPF), 1 M LiFSI/DME (1M), 4 M LiFSI/DME (4M), and LiFSI-1.2 DME-3 TTE by molar ratio (LHCE) electrolytes. The error bars of XPS results are calculated from the analysis of three different spots of the same sample. Spearman rank correlation coefficient<sup>41</sup> ( $\rho$ ) is calculated from the average values of the CE and F/C ratio.